cogent chemistry

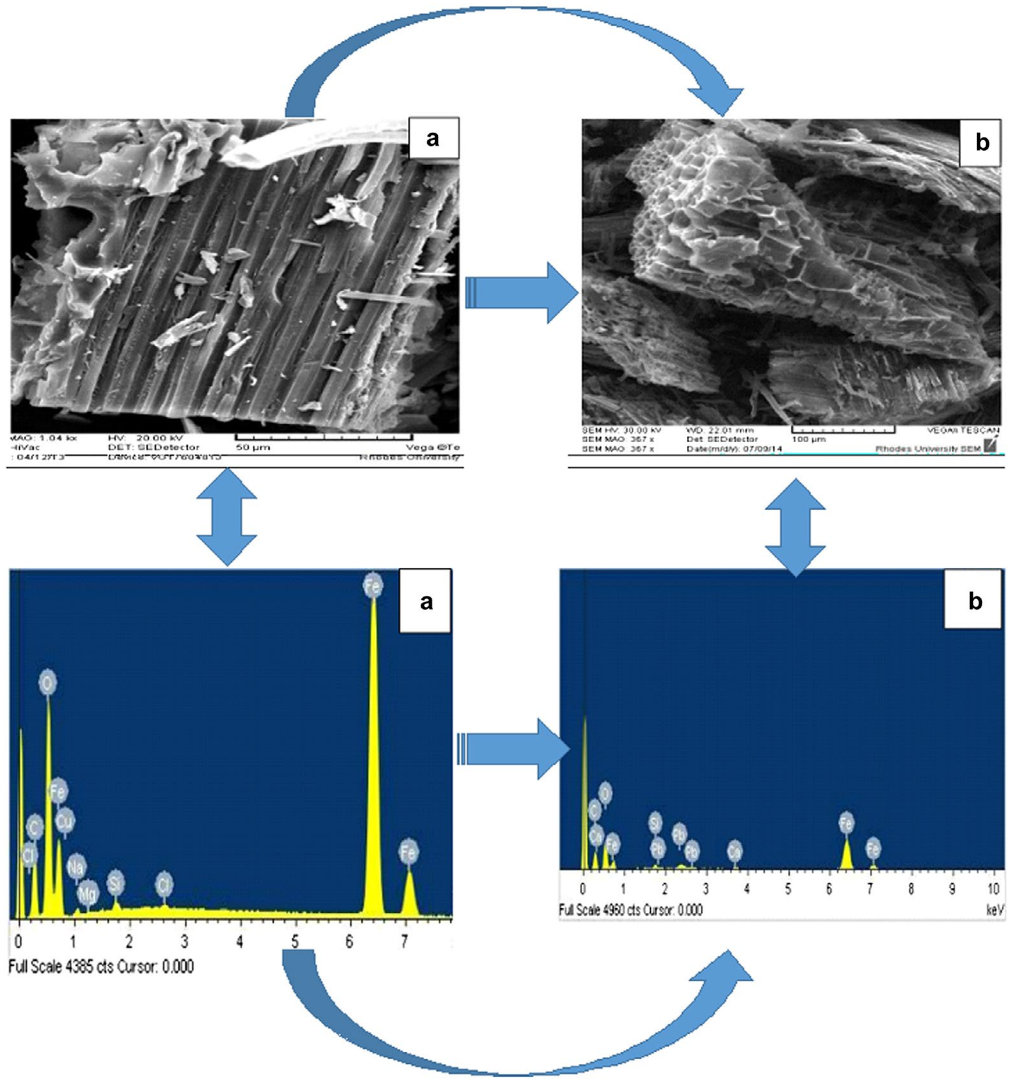


MATERIALS CHEMISTRY | RESEARCH ARTICLE

# Kinetics, mechanism, isotherm and thermodynamic studies of liquid-phase adsorption of Pb2+ onto wood activated carbon supported zerovalent iron (WAC-ZVI) nanocomposite

Adewumi O. Dada, Folahan A. Adekola and Ezekiel O. Odebunmi

*Cogent Chemistry* (2017), 3: 1351653

Dada et al., *Cogent Chemistry* (2017), 3: 1351653
https://doi.org/10.1080/23312009.2017.1351653

cogent chemistry



MATERIALS CHEMISTRY | RESEARCH ARTICLE

# Kinetics, mechanism, isotherm and thermodynamic studies of liquid-phase adsorption of $Pb^{2+}$ onto wood activated carbon supported zerovalent iron (WAC-ZVI) nanocomposite

Adewumi O. Dada[1]*, Folahan A. Adekola[2] and Ezekiel O. Odebunmi[3]

Received: 30 December 2016
Accepted: 03 July 2017
Published: 17 July 2017

*Corresponding author: Adewumi O. Dada, Department of Physical Sciences, Industrial Chemistry, Landmark University, P.M.B. 1001, Omu-Aran, Kwara State, Nigeria
E-mails: dada.oluwasogo@lmu.edu.ng, dada.oluwasogo@landmarkuniversity.edu.ng

Reviewing editor:
Young-Seok Shon, California State University, Long Beach, USA

Additional information is available at the end of the article

**Abstract:** The kinetics, mechanism, isotherm, and thermodynamics of adsorption of $Pb^{2+}$ onto wood-activated carbon-supported zerovalent iron (WAC-nZVI) nanocomposite was successfully studied. WAC-nZVI was characterized by a combination of spectroscopic and analytical techniques (BET, PZC, FTIR, SEM, and EDX). BET surface area was 101.50 $m^2/g$ and BJH Adsorption average pore diameter 116.73 Å. The adsorption of $Pb^{2+}$ studied in batch process depends on various operational parameters ranging from effect of pH to ionic strength. Kinetics data were best described by pseudo-second-order model based on high initial adsorption rate, $h_2$ (166.67 $mgg^{-1}$ $min^{-1}$) and correlation coefficient ($R^2 > 0.99$). The mechanism was controlled by both external and intraparticle diffusion models confirmed by Bangham and Boyd models. Equilibrium data were fitted to seven isotherm models. The Langmuir monolayer adsorption capacity (77.52 $m^2/g$) surpassed those previously investigated for adsorption of $Pb^{2+}$ onto nanoadsorbents. Validity of kinetics and isotherm models was studied using three statistical models. Post-adsorption characterization by SEM, EDX, and FTIR confirmed the presence of $Pb^{2+}$ on the loaded-WAC-nZVI.

Adewumi O. Dada

## ABOUT THE AUTHOR

Adewumi O. Dada is a lecturer in Landmark University, Department of Physical Sciences, Industrial Chemistry Program. He completed his PhD in the Department of Chemistry, University of Ilorin in 2015. His research areas are: Nanotechnology, Green Synthesis of Nanoparticles, Adsorption, Waste water treatment; Dyes and Heavy metals. He is a member of two research clusters in his home institution and some Academic Professional bodies. He was ranked 293rd position in Google scholar citation on the list of 600 scientists in Nigerian institutions in 2015 and constantly spotted as researcher with most cited article in Landmark University by Researchgate. He has published in peer-reviewed journals. He is an invited reviewer to some journals such as: *Materials Letters* (Elsevier), *Colloids and Surfaces A: Physicochemical & Engineering Aspects* (Elsevier), *Reviews in Chemical Engineering* (DE GRUYTER), *Applied Nanoscience* (Springer), and *Journal of Bioremediation* (Taylor and Francis). He is currently working on synthesis of novel nanocomposites and their applications in industrial effluent treatment.

## PUBLIC INTEREST STATEMENT

The release of heavy metal ions into the environment via unguided and unguarded anthropogenic activities remains ubiquitous challenge for the past decade. Lead is a hazardous metal well known for environmental contamination and health problems in many parts of the world. Its potential sources are reported in this article. WHO revealed that childhood lead exposure is estimated to contribute to about 600,000 new cases of children developing intellectual disabilities every year and also account for 143,000 deaths per year with the highest burden in developing countries; 4% of the global burden of ischemic heart disease; 5% of the global burden of stroke and there is no known level of lead exposure that is considered safe. This article has currently investigated the solution for water contaminated with lead ions using wood-activated carbon-supported zerovalent iron (WAC-nZVI) nanocomposite via adsorption as a low-cost and efficient technique. The outcome of this was validated.

Thermodynamic parameters ($\Delta H^o$, $\Delta S^o$, $\Delta G^o$) confirmed the feasibility, spontaneity, and randomness of the adsorption process. This study revealed a great potential of novel WAC-nZVI in effective removal of $Pb^{2+}$ from waste water.

**Subjects: Environment & Agriculture; Bioscience; Earth Sciences; Environmental Studies & Management; Food Science & Technology; Physical Sciences; Engineering & Technology; Health and Social Care**

**Keywords: novel nanocomposite (WAC-nZVI); $Pb^{2+}$ adsorption; kinetics and isotherm; statistical validity; thermodynamics**



## 1. Introduction

The release of heavy metal ions into the environment via unguided and unguarded anthropogenic activities remains ubiquitous challenge for the past decade. Lead is a hazardous metal well known for environmental contamination and health problems in many parts of the world. It can be potentially found in sources such as gold-leaded soil, hair dye, batteries, paints, pesticide, canned food, plants grown around industrial areas, cosmetics, tobacco smoke, ammunition (*1*). It is an accumulative toxicant that adversely affects copious body system such as neurologic, hematologic, gastrointestinal, cardiovascular, and renal systems. Those highly vulnerable to this hazardous effect are children and there are recent reports of some outbreaks in some areas in West Africa such as seen in Niger and Zamfara States of Nigeria (*2, 3*). Report from WHO revealed that childhood lead exposure is estimated to contribute to about 600 000 new cases of children developing intellectual disabilities every year, and also account for 143 000 deaths per year with the highest burden in developing countries; 4% of the global burden of ischemic heart disease; 5% of the global burden of stroke and there is no known level of lead exposure that is considered safe. However, the dose–response analyses conducted by the Joint Food and Agriculture Organization of the United Nations (FAO)/WHO Expert Committee concluded that permissible level of lead in drinking water and air are 10 μg/l and 0.5 μg/m$^3$ (*4,5*). Quite a number of conventional technologies such as ion exchange, solvent extraction, electrodialysis, reverse osmosis, ultrafiltration, cementation, chemical precipitation (*6*) have been used, however, adsorption has proven to be efficient, simple, explicit, cost-effective, and readily available technique of immobilization of heavy metals and dyes from the environment.

Several bioadsorbents have been reported for adsorption of $Pb^{2+}$ such as acid-modified rice husk (*6*); citric acid-modified clam shells (*7*), peat moss and peat moss-derived biochar (*8*); activated carbon made from sewage sludge (*9*), kaolin- and graphene-supported nZVI (*10, 11*), carbon-supported nanoscale zerovalent iron particles (*12*); granular activated carbon/zerovalent iron (*13*) but at the advent of nanoscience, researchers have been exploring the use of nanoadorbents due to their high surface area, effectiveness, and rapid adsorption than several bioadsorbents. The current trend in nanoscience research is the impregnation of nanoparticles into low-cost adsorbent in order to increase its efficiency. This is one of the primary focuses of this research. Hence, the quest for efficient adsorbent for uptake of toxic $Pb^{2+}$ propelled the research into the development of nanocomposite by impregnation and bottom-up approach. Activated carbon has been identified as effective adsorbents for pollutants removal. However, its application is still resisted because of some limitations such as availability, quality, and, most especially, its high cost in the developing countries. This has instigated us to explore the use of locally available material (Wood of *Cholophoral Excelsa* which is readily available in South-west Nigeria) for preparation of activated carbon and we further explored the opportunity of improving its adsorption capacity by impregnating it with iron nanoparticle via bottom-up approach by chemical reduction in a single-pot system. The two main approaches used in nanotechnology are “bottom–up” and “top–down.” In the “bottom-up” approach, materials, and devices are built from molecular components which assemble themselves chemically by principles of molecular recognition (*14*). It is a synthesis approach where the precursors or the building blocks are added onto the substrate to form the nanostructure substances.

To the best of our knowledge, there has not been any report on nZVI impregnated on activated carbon from readily available low-cost wood of *Cholophoral Excelsa* abundant in Africa. Based on the literature report and to the best of our understanding, there has never been any report on the material—raw wood dust of *cholophoral excelsa.* Other researchers used commercial activated, however, this present study produced activated carbon from neglected *cholophoral excelsa* and incorporated zerovalent iron nanoparticles into it forming activated carbon iron-coated zerovalent iron nanocomposite**.** Therefore, the objectives of this research are: (i) Bottom-up approach preparation of wood-activated carbon (WAC)-supported nanoscale zerovalent iron (nZVI) and characterization using Brunauer–Emmett–Teller (BET) and Barrett–Joyner–Halenda (BJH); point of zero charge (PZC); Fourier transform infrared spectroscopy (FTIR), scanning electron microscopy (SEM), energy-dispersive X-ray (EDX), and transmission electron microscope (TEM); (ii) investigation of the effect of adsorption functional parameters—pH, ionic strength, adsorbent dose, contact time, initial concentration, and temperature; (iii) determination of the kinetic and rate-controlling step (mechanism) using eight models—pseudo-first- and -second-order models, Elovich, fractional power, intraparticle diffusion, Spahn and Schlunder Model (external diffusion), Bangham and Boyd models, (iv) analyzing equilibrium data with seven isotherm models—Langmuir, Freundlich, Temkin, Dubinin–Raduskevich (D-R), Halsey, Harkin–Jura, and Jovanovic (v), and determination of randomness, spontaneity, and feasibility of the adsorption process using thermodynamic parameters—change in standard enthalpy ($\Delta H°$), entropy ($\Delta S°$), and Gibb's free energy ($\Delta G°$).

## 2. Materials and methods

### *2.1 Materials*

All the reagents used were of analytical grade mostly purchased from Sigma-Aldrich, USA, namely: sodium borohydride ($NaBH_4$) (for the chemical reduction), ferric chloride ($FeCl_3$), $HNO_3$, and NaOH. Absolute ethanol from BDH, while raw wood dust of *Cholophoral excelsa*, was obtained at sawmill workshop close to Landmark University campus.

### *2.2. Methods and characterization*

#### *2.2.1. WAC-nZVI nanocomposite preparation*

Preparation of novel WAC-nZVI was carried out using two precursors: (A) nanoscale zerovalent iron, ZVI and (B) wood-activated carbon, WAC. The precursor B was prepared following the previously work by Dada et al. (15) and kept in the desiccator for further use. In a distinctive procedure for the preparation of WAC-nZVI, excess borohydride is important for better formation of iron nanoparticle. Therefore, a carefully weighed amount of precursor B was initially introduced into 0.023 M $FeCl_3$ and homogenized for 3 h using a magnetic stirrer. Thereafter, 0.123 M $NaBH_4$ was introduced to 0.023 M $FeCl_3$ in ratio 5:1 under nitrogen-controlled glove box single-pot system giving WAC-nZVI (black) was obtained. The impregnation of wood-activated carbon-supported zerovalent iron nanocomposite (WAC-nZVI) was carried out modifying similar procedure reported in our previous studies (16–18) and equation of reaction is as stated in Equation (1):

$$WAC + 4Fe^{3+} + 3BH_4^- + 9H_2O \rightarrow WAC - 4Fe \downarrow + 3H_2BO_3^- + 12H^+ + 6H_2 \uparrow \quad (1)$$

WAC-nZVI was thereafter kept in a desiccator for further characterization and adsorption studies.

#### *2.2.2. Characterization*

BET surface area was determined using Micrometritics AutoChem II Chemisorption Analyzer. Point of zero charge (PZC) was determined by modifying the procedure reported by Srivastava et al. (19). Morphology and elemental constituents were determined using scanning electron microscopy (SEM) integrated with energy-dispersive X-ray (EDX) using a TESCAN Vega TS 5136LM typically at 20 kV at a working distance of 20 mm with samples coated in a Golden Balzers' Spluttering device and functional groups were determined by Fourier transform infrared spectroscopy (FTIR) using Schimadzu FTIR model IR 8400S.

*2.2.3. Adsorption experiment*

*2.2.3.1. Batch equilibrium studies:* Sorption experiment was done by agitating 100 mg of the WAC-nZVI with 50 $cm^3$ of different initial $Pb^{2+}$ concentrations from 10 to 200 ppm in 60 $cm^3$ of Teflon bottle intermittently for 3 h. The combination was filtered and the filtrate was immediately analyzed in triplicate for residual $Pb^{2+}$ ions concentrations using atomic absorption spectrophotometer (AAS). The mean value of the residual $Pb^{2+}$ concentration for each set of the experiments was calculated and used. Adsorption operational parameters such as effect of pH, contact time, initial concentration, adsorbent dose, temperature, and ionic strength were investigated following a similar procedure (18, 20–22).

### 2.3. Adsorption analysis

*2.3.1. Quantity adsorbed and removal efficiency*
Quantity of $Pb^{2+}$ adsorbed ($q_e$), removal efficiency, and error analysis were calculated using Equations (2)–(6). Adsorption capacities and the removal efficiency were obtained using Equations (2) and (3), respectively (22, 23):

$$q_e = \frac{(C_o - C_e)V}{W} \tag{2}$$

$$\%\, E = \frac{C_o - C_e}{C_o} \times 100 \tag{3}$$

*2.3.2. Sum of Square Error (SSE), Chi-square test ($\chi^2$) and Normalized Standard Deviation ($\Delta q$) Statistical Validity*
The best fit, suitability, and agreement of kinetic and isotherm models were validated using three statistical models: sum of square error (SSE), chi-square test ($\chi^2$), and normalized standard deviation ($\Delta q$).

The sum of square error (SSE) is mostly used by researchers with the mathematical expression given in Equation (4):

$$\mathrm{SSE} = \sum_{i=1}^{n} \left(q_{e,\mathrm{cal}} - q_{e,\mathrm{exp}}\right)^2 \tag{4}$$

Better agreement between the experimental quantity adsorbed and the calculated quantity adsorbed can be judged using this tool (24).

The chi-square test measures the difference between the experimental and calculated quantities adsorbed ($q_{e,\mathrm{exp}}$ and $q_{e,\mathrm{cal}}$, respectively). Magnitude of the value of chi-square depends on the agreement between the $q_{e,\mathrm{exp}}$ and the $q_{e,\mathrm{cal}}$. If data evaluated from the model are similar to experimental data, $\chi^2$ would be small and if they differ, $\chi^2$ will be large (25).

$$\chi^2 = \sum_{i=1}^{n} \frac{\left(q_{e,\mathrm{exp}} - q_{e,\mathrm{cal}}\right)^2}{q_{e,\mathrm{cal}}} \tag{5}$$

The normalized standard deviation $\Delta q$ (%) was evaluated using Equation (6).

$$\Delta q(\%) = 100 \frac{\sqrt{\sum_{i=1}^{n} \left(\frac{q_{e,\mathrm{exp}} - q_{e,\mathrm{cal}}}{q_{e,\mathrm{exp}}}\right)^2}}{n-1} \tag{6}$$

where $n$ is the number of data points and other parameters are the same as earlier defined. Lower value of $\Delta q$ indicates good fit between experimental and calculated data (26).

## 3. Results and discussion

### 3.1. Characterization (BET, BJH, PZC, FTIR, SEM–EDX)

The following physicochemical properties of the WAC-nZVI nanocomposite vis-à-vis surface area, micropore area, BJH adsorption cumulative surface area of pores, pore volume, pore diameter, pore width, average particle size by Brunauer–Emmett–Teller (BET) and Barrett–Joyner–Halenda (BJH). The point of zero charge is of basic importance in surface science. The point of zero charges obtained for WAC-nZVI revealed that adsorption of $Pb^{2+}$ would take place at a pH > $pH_{(pzc)}$ (19,27). The result presented in Table 1 showed that adsorption of $Pb^{2+}$ was favorable at a pH above PZC (Figure S1).

The relatively higher values of the external surface area compared to the micropore surface area implies that WAC-nZVI utilized its external surfaces for adsorption than its micropore surfaces (21).

Figure 1(a) and (b) depict the FTIR spectra of wood dust-activated carbon-supported iron nanocomposite (WAC-nZVI) before and after adsorption of $Pb^{2+}$. Stated in Table 2 are important FTIR bands of WAC-nZVI with their possible functional groups assigned before and after $Pb^{2+}$ adsorption. The reduction in vibration band intensities after adsorption is a confirmation of participation of functional group in adsorption process.

Revealed in Figure 2(a) is the scanning electron microscopy (SEM) image of WAC-nZVI nanocomposite before adsorption. The surface was fibrous, cellulosic fiber flat-like, straight lamina showing the evidence of pores of activated cell wall of plant of *Chlorophora excelsa* and indication of zerovalent iron nanoparticle with surface area of BET 101.5033 $m^2/g$, pore volume 0.056673 $cm^3/g$, pore width 22.3334 Å, pore diameter 116.727 Å. The lamina structural nature of WAC-nZVI enhanced the flow of $Pb^{2+}$ into the pores of WAC-nZVI. These characteristics boosted the performance of WAC-nZVI in the immobilization of $Pb^{2+}$ as supported by the findings in previous work by Dada et al. (17) and Anees et al. (28). A change in morphology which is attributed by the robustness and swollen of WAC-nZVI after $Pb^{2+}$ adsorption was confirmed by the SEM analysis in Figure 2(b)

**Table 1. Physicochemical properties of WAC-nZVI nanocomposites**

| Physicochemical properties | WAC-nZVI |
|---|---|
| *pH* | 7.53 |
| *PZC* | 5.60 |
| *BET surface area* | 101.5033 $m^2/g$ |
| *t*-Plot micropore area | 78.6414 $m^2/g$ |
| *t*-Plot external surface area | 22.8619 $m^2/g$ |
| BJH adsorption cumulative surface area of pores between 17.000 and 3,000.000 Å diameter | 8.389 $m^2/g$ |
| *Pore volume* | |
| Single-point adsorption total pore volume of pores less than 1,094.743 Å diameter at P/Po = 0.981990668 | 0.056673 $cm^3/g$ |
| *t*-Plot micropore volume | 0.036247 $cm^3/g$ |
| BJH Adsorption cumulative volume of pores between 17.000 and 3,000.000 Å diameter | 0.024482 $cm^3/g$ |
| *Pore size* | |
| Adsorption average pore width (4 V/A by BET) | 22.3334 Å |
| BJH Adsorption average pore diameter (4 V/A) | 116.727 Å |

**Figure 1. FTIR spectra for (a) WAC-nZVI before adsorption and (b) Pb–WAC-nZVI after adsorption.**

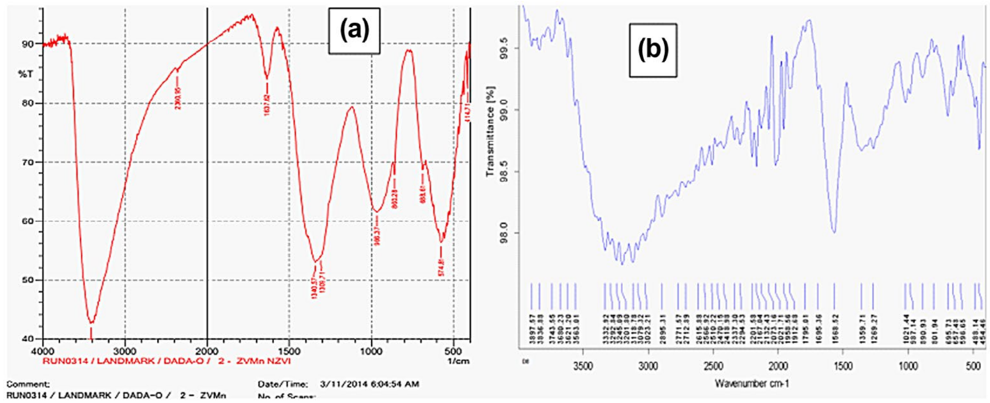


**Table 2. Important FTIR bands of WAC-nZVI with their possible functional groups before and after $Pb^{2+}$ adsorption**

| Functional group(s)/peaks | | Intensities | |
|---|---|---|---|
| **Functional group(s)** | **Vibration bands/ peaks ($cm^{-1}$)** | **WAC-nZVI before adsorption** | **Pb(II)-loaded WAC-nZVI after adsorption** |
| O–H stretching | 3,417.98 | 42.474 | 3 |
| H–O–H bending | 1,637.62 | 84.066 | 2.5 |
| C=C | 1,340.57–1,309.71 | 53.881 | 0 |
| Si–O–Al | 966.37 | 61.453 | 1.5 |
| C–O | 860.28 | 67.45 | 1 |
| $Fe^0$ | 688.61 | 68.624 | 1.02 |
| | 574.81 | 56.232 | 0.5 |
| | 414.71 | 82.49 | 1.5 |

**Figure 2. SEM images of (a) WAC-nZVI before adsorption and (b) Pb–WAC-nZVI after adsorption.**

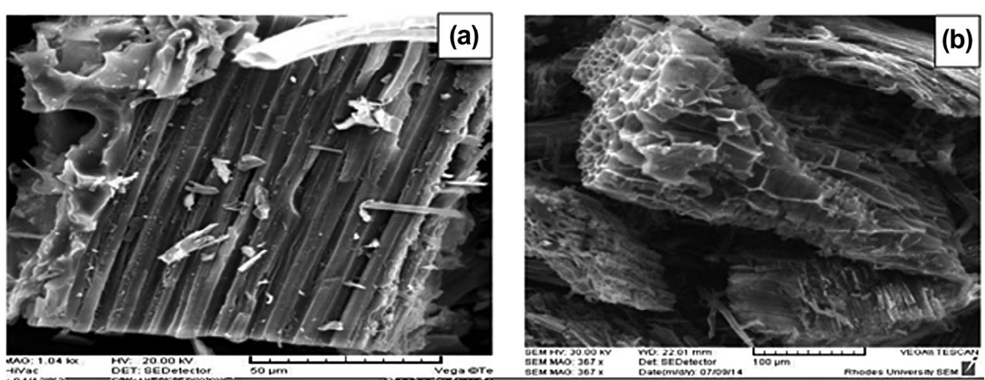


In order to further confirm $Pb^{2+}$ adsorbed onto WAC-nZVI, energy-dispersive X-ray (EDX) studies of WAC-nZVI before and after adsorption was carried out. The EDX spectra give the characteristic peaks of the nanoparticles and the information on the surface atomic distribution. EDX spectra of (a) WAC-nZVI before and (b) loaded Pb–WAC-nZVI after adsorption are revealed in Figure 3(a) and (b). The EDX spectrum in Figure 3(a) revealed the intense peaks of the core shell zerovalent iron and other elemental constituents before adsorption which was supported by the FTIR result. Other elements present could be traceable to the additives during the course of the analysis. In most metal adsorption studies, the residual concentration was determined by atomic adsorption spectroscopy (AAS). This could not

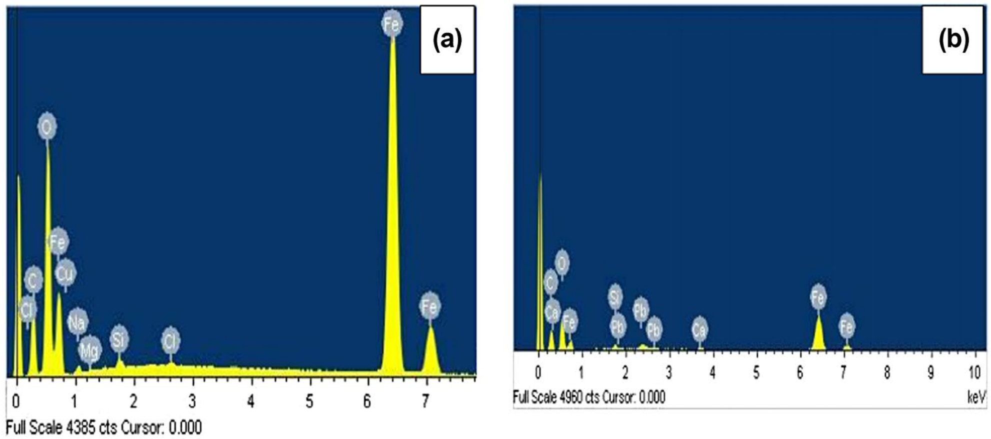


**Figure 3. EDX analysis of (a) WAC-nZVI before adsorption and (b) Pb–WAC-nZVI after adsorption.**

prove the presence of the metal ions on the adsorbent. However, the presence of $Pb^{2+}$ on WAC-nZVI as seen in the EDX spectrum in Figure 3(b) was an evidence of the adsorption of $Pb^{2+}$ onto WAC-nZVI.

### *3.2. Influence of pH, adsorbent dose, and contact time*

The pH of the solution in adsorption studies influences both the chemistry of solution and surface charge of the adsorbents (*29, 30*). Investigation of the effect of pH was carried out between the pH ranges 1–8. $Pb^{2+}$ in solution exits as $Pb^{2+}$, $Pb(OH)^{+}$, $Pb(OH)_2$ in acidic medium causing electrostatic competition between $Pb^{2+}$, $H^{+}$, and other cationic species as a result of protonation leading to low removal efficiency and quantity adsorbed as seen in Figure 4. However, as the pH increases tending toward pH 6, increase in quantity of $Pb^{2+}$ adsorbed was evident due to the decrease in electrostatic repulsion, low competition among positive ions, and availability of active sites for adsorption. The optimum percentage of $Pb^{2+}$ removed was attained at pH 6 which was corroborated by the findings of Xu et al. (*31*) and Pirouz et al. (*32*).

The interaction between the $Pb^{2+}$ ions and WAC-nZVI was maximized by the investigation of the effect of adsorbent dose on the uptake of $Pb^{2+}$. The percentage removal efficiency increases with the increase in adsorbent dose because of the increase in number of active sites as revealed in Figure 5. At 10 mg WAC-nZVI, 51.73% $Pb^{2+}$ was adsorbed, while at 100 mg 97.3% was adsorbed until a saturated point was reached when no significant increase in the removal efficiency was attained based on limited number of active sites. This performance confirmed the efficacy of the nanocomposite prepared being a blend of activated carbon (WAC) from neglected material and zerovalent iron nanoparticles (nZVI). However, the quantity adsorbed on WAC-nZVI is a measure of the occupancy capacity of the adsorbent. Obviously, at 10 mg, 93.71 mg $Pb^{2+}$ was attained and this decreased with decrease in the number of active sites. Other factors responsible for this are: interference between binding sites and higher adsorbed dose; insufficiency of $Pb^{2+}$ ions in solution with respect to available binding sites; aggregation arising from high sorbent dose leading to decrease in total surface area of adsorbent and an increase in diffusional path length and unsaturation of the adsorption sites during the adsorption reaction. This finding is supported by the previous work of Gong et al. (*33*).

**Figure 4. The effect of pH on $Pb^{2+}$ adsorbed onto WAC-nZVI.**

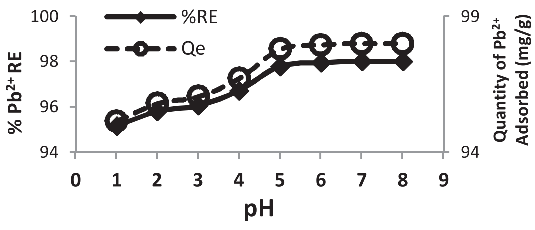


Notes: Experimental conditions: Pb2+ Concentration= 200 mg/L; *WAC-nZVI dose = 100 mg* ; Volume of Pb2+ solution = 50 mL; Stirring speed = 200 rpm; Contact time = 30 min, and Temperature = 25± 2°C.

**Figure 5. Effect of WAC-nZVI dose on $Pb^{2+}$ adsorbed.**

Notes: Experimental conditions: $Pb^{2+}$ Concentration = 200 mg/L; Volume of $Pb^{2+}$ solution = 50 mL; pH = 6, Stirring speed = 200 rpm; Contact time = 30 min, and Temperature = 25± 2°C.

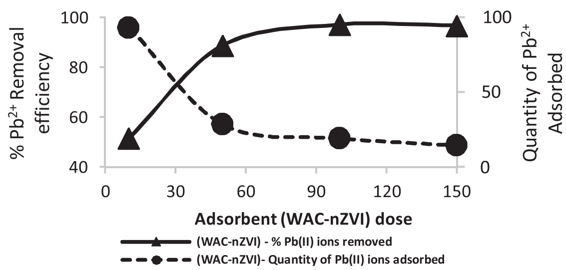


The build-up of charges around the adsorbent in a solid–liquid system takes time. Therefore, effect of contact time was investigated as one of the factors affecting the immobilization of $Pb^{2+}$ onto WAC-nZVI. The effect of contact time was studied at contact time of 10–120 min at optimum conditions. Figure 6 showed a rapid increase in contact time at the first 10–30 min into the adsorption process. However, a steep and uninterrupted step was observed between 30 and 60 min, while the graph leveled off for 120 min without a significant change in the quantity adsorbed (18).

### *3.3. Batch kinetic studies and statistical validity*

Data from kinetic experiment were subjected to eight kinetic and mechanism models.

#### *3.3.1. Pseudo-first-order (Lagergren's rate equation)*

The Lagergren's rate equation of pseudo-first order is given in Equation (7) (*34, 35*):

$$\log(q_e - q_t) = \log\ q_e - \frac{k_1 t}{2.303} \tag{7}$$

$$h_1 = k_1 q_e \tag{8}$$

Equation (8) defines $h_1$ the initial adsorption rate from pseudo-first-order rate equation, the plot of $\log(q_e - q_t)$ versus $t$ gave a linear relationship (Figure 7), where $k_1$ and $q_e$ were determined from the slope and intercept of the linear plot (Figure 7(a))

**Figure 6. Effect of contact time on $Pb^{2+}$ adsorbed onto WAC-nZVI .**

Notes: Experimental conditions: Pb2+ Concentration= 200 mg/L; WAC-nZVI dose = 100 mg ; Volume of Pb2+ solution = 50 mL; Stirring speed = 200 rpm; Temperature = 25± 2°C.

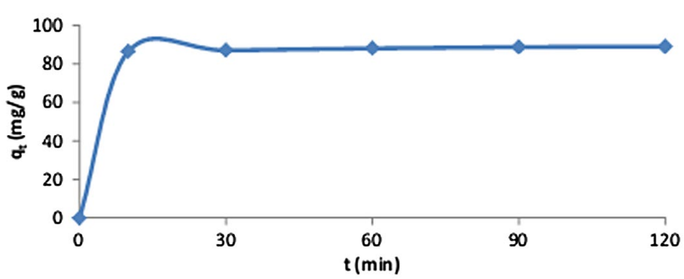


**Figure 7. (a–d): Linear plots of (a) Pseudo-first-order, (b) Pseudo-second-order, (c) Elovich, (d) Fractional power.**

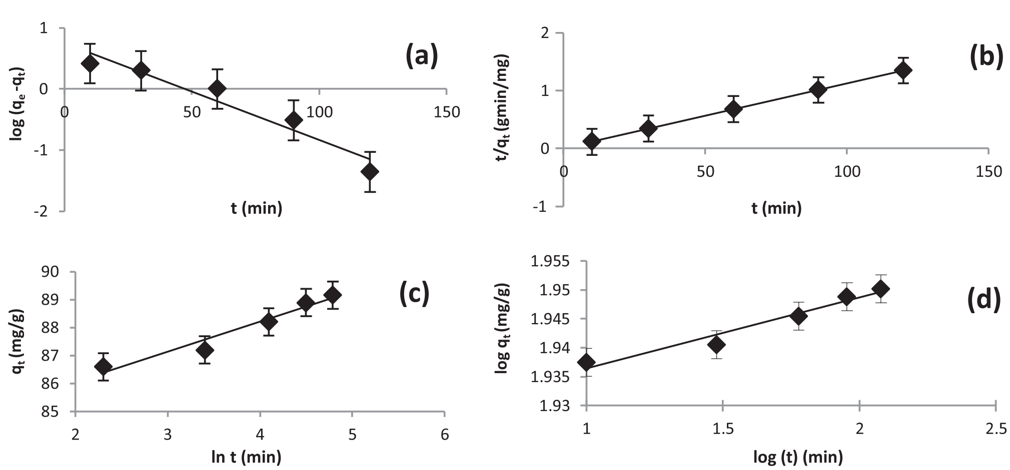

Solid–liquid interaction of WAC-nZVI and $Pb^{2+}$ is suggesting that one $Pb^{2+}$ is adsorbed on the surface of one WAC-nZVI as demonstrated in Equation (9):

$$WAC + Pb^{2+}_{aq} \xrightarrow{k_2} WAC \bullet Pb_{solid\ phase} \tag{9}$$

From evaluated parameters presented in Table 3, it is obvious that $q_{e,exp} = 89.2$ mgg$^{-1}$ and $q_{e,cal} = 5.572$ mgg$^{-1}$ coupled with regression coefficient, $R^2 < 0.95$ and larger values of sum of square error (SSE), chi-square test ($\chi^2$), and normalized standard deviation ($\Delta q$). These results as well as lower value of $h_1 = 0.193$ mgg$^{-1}$ min$^{-1}$ showed that kinetics of liquid-phase adsorption of $Pb^{2+}$ onto WAC-nZVI did not fit well to pseudo-first order.

### 3.3.2. Pseudo-second order

This model adopts that one $Pb^{2+}$ is sorbed onto two sorption sites on WAC-nZVI nanocomposites' surface according to Equation (10):

$$2WAC + Pb^{2+}_{aq} \xrightarrow{k_2} WAC_2 \bullet Pb_{solid\ phase} \tag{10}$$

Evidence of chemisorption mechanism is substantiated in the pseudo-second-order model (Equation (11)) (*16, 30, 36*):

$$\frac{t}{q_t} = \frac{1}{h_2} + \frac{1}{q_e}t \tag{11}$$

$$h_2 = k_2 q_e^2 \tag{12}$$

Defined in Equation (12) is pseudo-second-order initial adsorption rate (mg$^2$/g$^2$ min). Linear plot of $t/q_t$ against $t$ in Figure 7(b), gave a straight line and evaluated data obtained are presented in Table 3. The linearity of the plot, close and good agreement between the calculated $q_e$ and $q_e$, experimental values (89.2 and 90.90, respectively), higher value of $h_2 = 166.67$ mg$^2$/g$^2$ min, correlation coefficients ($R^2 > 0.99$), and lower values of the validity models are strong clues of the applicability of pseudo-second-order model. It is suggested that the kinetic of adsorption of $Pb^{2+}$ onto WAC-nZVI was best described by pseudo-second-order model supporting chemisorption process.

### 3.3.3. Elovich model

Equation (13) described the Elovich model as:

$$q_t = \frac{1}{\beta}\ell n(\alpha\beta) + \frac{1}{\beta}\ell n(t) \tag{13}$$

**Table 3. Adsorption kinetic models' parameters for the sorption of $Pb^{2+}$ onto WAC-nZVI**

| Pseudo-first-order | WAC-nZVI | Pseudo-second-order | | Elovich | | Fractional power | |
|---|---|---|---|---|---|---|---|
| $k_1$ (min$^{-1}$) | 0.035 | $k_2$ (g/mg/min) | 0.020 | α (g.min$^2$/mg) | $1.60 \times 10^{+34}$ | $v$ (min$^{-1}$) | 0.012 |
| $h_1$ (mg/g/min) | 0.193 | $h_2$ (mg/g/min) | 166.667 | $\beta$ (g.min/mg) | 0.933 | $k_3$ (mg/g) | 83.946 |
| $R^2$ | 0.932 | $R^2$ | 1.000 | $R^2$ | 0.953 | $R^2$ | 0.954 |
| SSE | 6993.642 | SSE | 2.921 | SSE | 0.026 | SSE | 0.0842 |
| $\chi^2$ | 1255.140 | $\chi^2$ | 0.032 | $\chi^2$ | $3 \times 10^{-4}$ | $\chi^2$ | 0.001 |
| $\Delta q$ | 23.438 | $\Delta q$ | 0.479 | $\Delta q$ | 0.0448 | $\Delta q$ | 0.081 |
| $q_{e,exp}$ (mg/g) | 89.200 | $q_{e,exp}$ (mg/g) | 89.200 | $q_{e,exp}$ (mg/g) | 89.200 | $q_{e,exp}$ (mg/g) | 89.200 |
| $q_{e,cal}$ (mg/g) | 5.572 | $q_{e,cal}$ (mg/g) | 90.909 | $q_{e,cal}$ (mg/g) | 89.040 | $q_{e,cal}$ (mg/g) | 88.909 |

The slope of $^1/_\beta$ and intercept $^1/_\beta \ell n(\alpha\beta)$ were determined from linear plot of $q_t$ vs. ln($t$) (Figure 7(c)). Regression coefficient, $R^2 > 0.95$ is close to unity, Elovich's constant, $\alpha = 1.60 \times 10^{+34}$ g min$^2$/mg defines the rate of reaction, $1/\beta$ value above unity reflects the number of sites available for adsorption, whereas the value of $1/\beta$ ln $(\alpha\beta) = 86.82$ mgg$^{-1}$ indicates the adsorption quantity when ln($t$) equals to zero (37). All these parameters revealed that Elovich model also better described the liquid-phase adsorption (30).

### 3.3.4. Fractional power

Equation (14) portrayed the fractional power model given as (18):

$$\log(q_t) = \log(k) + v\log(t) \tag{14}$$

where $v$ is a positive constant less than unity ($v = 0.012$ min$^{-1}$) displaying the time dependence of liquid-phase adsorption of $Pb^{2+}$ onto WAC-nZVI. The $k = 83.9$ mgg$^{-1}$ was determined from slope and intercept of a linear plot of log ($q_t$) vs. log ($t$) (Figure 7(d)) suggesting the strength of the site for $Pb^{2+}$ immobilization. The lower values of SSE, $\chi^2$, and $\Delta q$ evaluated as 0.0842, 0.001, and 0.081, respectively, validated the appropriateness of fractional power in describing the time dependence of adsorption process (38).

## 3.4. Adsorption mechanism

The adsorption mechanisms, the rate-controlling steps were determined using intraparticle diffusion, external diffusion, Bangham and Boyd models. Their mathematical expressions are given in Equations (15)–(20) (17, 39):

Intraparticle diffusion (Morris and Weber model) (40):

$$q_t = k_{id}t^{0.5} + C \tag{15}$$

External diffusion (Spahn and Schlünder model):

$$\ln\left[\frac{C_t}{C_o}\right] = -k_{ext}\left(\frac{A}{V}\right)t \tag{16}$$

A/V is external adsorption area to the total solution volume, and $t$ is sorption time.

Bangham model:

$$\log\log\left(\frac{C_o}{C_o - q_t m}\right) = \log\left(\frac{k_o m}{2.303V}\right) + \alpha\log(t) \tag{17}$$

where $\alpha$ and $K_o$ are the constants and $t$ is the contact time (min).

Boyd model:

$$F = 1 - \left(^6/_{\pi^2}\right)\exp(-B_t) \tag{18}$$

$$F = \frac{q_t}{q_e} \tag{19}$$

where $q_t$ is the amount of the $Pb^{2+}$ adsorbed at time t (mg/g) and $q_e$ is the amount of the $Pb^{2+}$ adsorbed at equilibrium (mg/g), $F$ is the fraction of $Pb^{2+}$ adsorbed at time t, and $B_t$ is the mathematical function of $F$. Substituting Equation (19) in (15), Equation (18) simplifies to:

$$B_t = -0.4977 - \ln(1 - F) \tag{20}$$

**Figure 8. (a–d) Linear plots of (a) Intraparticle Diffusion, (b) External Diffusion, (c) Bangham, and (d) Boyd mechanism models for adsorption of $Pb^{2+}$ onto WAC-nZVI.**

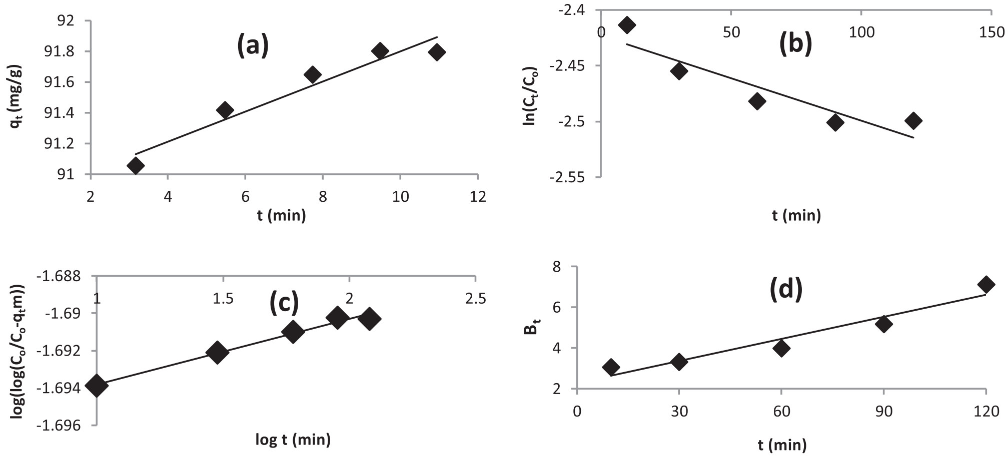


**Table 4. Adsorption mechanism models for immobilization of $Pb^{2+}$ onto WAC-nZVI**

| Intraparticle diffusion | WAC-nZVI | External diffusion | | Bangham | | Boyd | |
|---|---|---|---|---|---|---|---|
| $k_{ip}$ (mg/g/min $^{0.5}$) | 0.348 | $k_{fd}$ | 0.002 | $K_o$ | 0.022 | $R^2$ | 0.933 |
| $C$ | 85.440 | | | $A$ | 0.012 | | |
| $R^2$ | 0.987 | $R^2$ | 0.967 | $R^2$ | 0.954 | | |

The calculated $B_t$ values were plotted against time $t$ (min). Depicted in Figure 8(a)–(d) are the linear plots of (a) intraparticle diffusion, (b) external diffusion (Spahn and Schlünder model), (c) Bangham, (d) Boyd adsorption mechanism models for adsorption of $Pb^{2+}$ onto WAC-nZVI. In this study, the intraparticle diffusion constant ($k_{id}$) and the thickness of the surface ($C$) were determined from the slope and intercept of linear plot of $q_t$ vs. $t^{0.5}$. The intercept ($C$ = 19.397) which is the thickness of the surface gives information about the contribution of the surface adsorption in the rate-determining step. The larger the intercept, the greater the contribution of the pore to adsorption (17). The plot (Figure 8(a)) not passing through the origin indicating that intraparticle diffusion is not the only rate-determining step (*26*). However, it is suggested that other step like external diffusion maybe involved in the rate-determining steps. Parameters of Spahn and Schlunder model were evaluated from the linear plot of $ln\ (C_t/C_o)$ vs. $t$ (Figure 8(b), Table 4)

More so, Bangham model was applied to confirm the intraparticle diffusion. The pore diffusion mechanism was further supported by double logarithm plot (Bangham model) since plot of $\log\log\left(\frac{Co}{Co-q_t m}\right)$ against $\log(t)$ gave a straight line (Figure 8(c)) with high correlation coefficient, $R^2 > 0.95$, *the values of* $\alpha$ and k less than unity (Table 4) and Boyd model with $R^2 < 0.95$. All these values are suggesting that intraparticle diffusion or pore diffusion is one of the rate-determining steps (*41*, *42*)

### *3.5. Equilibrium studies and isotherm models*

#### *3.5.1. Initial concentration*

The initial $Pb^{2+}$ concentration constitutes a significant driving force allowing the ionic mass transfer between the aqueous and the solid phases (*43*). Effect of initial concentration plays one of the major roles in the uptake of $Pb^{2+}$. The concentration range of 10–200 mg/L was investigated at optimum conditions. Specifically, the increase in adsorption capacity with an increase in concentration is due to the concentration gradient developed at solid–solution interface. At higher concentration of $Pb^{2+}$, the active sites of WAC-nZVI were bombarded by more of $Pb^{2+}$ as the process continued until a saturated point was reached. The quantity adsorbed increased with an increase in initial concentration

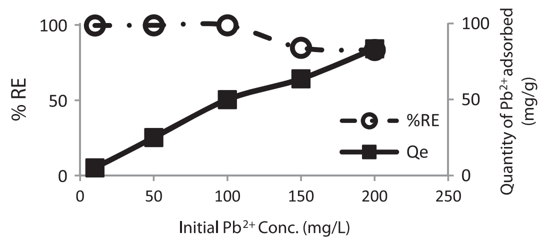


**Figure 9. Percentage and quantity of $Pb^{2+}$ adsorbed onto WAC-nZVI at various initial $Pb^{2+}$ concentrations.**

due to the availability of the active sites as revealed in Figure 9. However, the percentage removal efficiency decreased with an increase in concentration because of decrease in the rate of binding of $Pb^{2+}$ to the active sites at the approach of equilibrium.

### *3.5.2. Adsorption isotherms and statistical validity*

In order to understand the interaction between WAC-nZVI and $Pb^{2+}$, the data obtained from equilibrium adsorption studies were analyzed using seven of two parameters isotherm models: Langmuir, Freundlich, Temkin, Dubinin–Raduskevich (D–R), Halsey, Harkin–Jura, and Jovanovic. Description of the interaction between WAC-nZVI and $Pb^{2+}$, estimation of the adsorption capacity, information about adsorption mechanisms, surface properties, and affinity of the adsorbent can be equally obtained from the evaluated parameters from these isotherm models. Based on the statistical model errors which are normally and independently distributed, all the isotherm models are subjected to three statistical errors analyses for validity test. Given in Table 5 are the isotherm models equations, their linear and nonlinear forms as seen in Equations (21)–(28) as well as the various parameters plotted. Presented in Figures 10 (a)–(g) are the corresponding linear plots for Langmuir, Freundlich, Temkin, Dubinin–Raduskevich (D–R), Halsey, Harkin–Jura, and Jovanovic isotherm models, respectively. The evaluated parameters of the isotherm models are well presented in Table 6.

Langmuir isotherm model is a semi-empirical isotherm derived from a proposed kinetic mechanism based on the assumptions that the surface is energetically homogeneous, and there is no interaction between neighboring adsorbed specie ($Pb^{2+}$), adsorption takes place only at specific localized sites on the surface and the saturation coverage corresponds to complete occupancy of these sites. Given in Table 5 are Langmuir equation and the expression for Langmuir separation factor as seen in Equations (22) and (23), respectively. The parameters $q_e$ and $C_e$ are the quantity of metal ions adsorbed (mg/g) and concentration (mg/L) at equilibrium, respectively, $q_{max}$ is the theoretical maximum monolayer sorption capacity (mg/g), and $K_L$ (L/g) represents the Langmuir isotherm constant. The essential features of the Langmuir isotherm may be expressed in terms of equilibrium parameter, $R_L$, which is a dimensionless constant referred to as separation factor.

**Table 5. Different adsorption isotherm models (*15, 21, 44–46*)**

| S/N | Isotherms | Nonlinear form | Linear form | Equations | Plots |
|---|---|---|---|---|---|
| 1 | Freundlich | $q_e = K_f C_e^{1/n_f}$ | $\log q_e = \log K_f + {}^{1}/_{n_f} \log C_e$ | (21) | $\log q_e$ vs. $\log C_e$ |
| 2 | Langmuir | $q_e = q_{max} \frac{K_L C_e}{1+K_L C_e}$ | $\frac{C_e}{q_e} = \frac{1}{K_L q_{max}} + \frac{C_e}{q_{max}} R_L = \frac{1}{1+K_L C_o}$ | (22) and (23) | $\frac{C_e}{q_e}$ vs. $C_e$ |
| 3 | Temkin | $q_e = \frac{RT}{b_T} \ln(A_T C_e)$ | $q_e = \frac{RT}{b_T} \ln A_T + \left(\frac{RT}{b_T}\right) \ln C_e$ | (24) | $q_e$ vs. $\ln C_e$ |
| 4 | Dubinin–Radushkevich (D–R) | $q_e = q_d \exp(-A_{DKR}\varepsilon^2)$ | $\ln q_e = \ln q_d - A_{DKR}\varepsilon^2$ $E = -\left[\frac{1}{\sqrt{2A_{D-R}}}\right]$ | (25) | $\ln q_e$ vs. $\varepsilon^2$ |
| 5 | Halsey | $q_e = Exp\left(\frac{\ln k_H - \ln Ce}{n_H}\right)$ | $\ell n q_e = \left[\left(\frac{1}{n_H}\right)\ell n K\right] - \left(\frac{1}{n_H}\right)\ell n C_e$ | (26) | $\ln q_e$ vs. $\ln C_e$ |
| 6 | Harkin–Jura | $q_e = \left(\frac{A}{B_2 - \log C_e}\right)^{1/2}$ | $\frac{1}{q_e^2} = \left[\frac{B}{A}\right] - \left[\frac{1}{A}\right] \log C_e$ | (27) | $\frac{1}{q_e^2}$ vs. $\log C_e$ |
| 7 | Jovanovic | $q_e = q_{max}\left(1 - \exp^{(K_j C_e)}\right)$ | $\ln q_e = \ln q_{max} - k_j Ce$ | (28) | $\ln q_e$ vs. $C_e$ |

**Figure 10. (a–e): Linear plots of (a) Freundlich, (b) Langmuir, (c) Temkin, (d) D-R, (e) Halsey (f) Harkin–Jura, (g) Jovanovic isotherm models for sorption of $Pb^{2+}$ onto WAC-nZVI, and (h) Plot of Langmuir dimensionless separation factor for adsorption of $Pb^{2+}$ onto WAC-nZVI.**

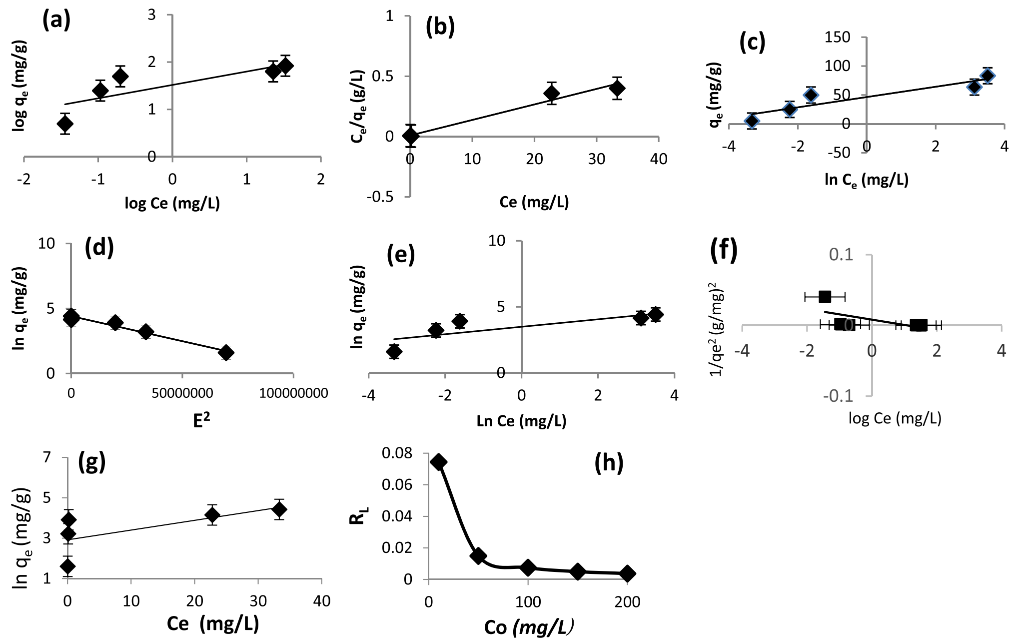


The equilibrium data were also best described by the Langmuir isotherm model with $R^2$ value of 0.9723 (Figure 1(a)). The maximum monolayer ($q_{max}$) $Pb^{2+}$ adsorption capacity obtained was 77.07 mg/g. The essential features of the Langmuir isotherm may be expressed in terms of dimensionless separation factor, $R_L$, given as (*30, 47*):

$$R_L = \frac{1}{1 + K_L C_o} \tag{23}$$

$R_L$ value indicates the adsorption nature to either unfavorable or unfavorable. It is unfavorable if $R_L > 1$, linear if $R_L = 1$, favorable if $0 < R_L < 1$, and irreversible if $R_L = 0$ (*15*). The value of $R_L$ which ranges between $7.44 \times 10^{-2}$ and $3.77 \times 10^{-3}$ (Figure 10(h)) indicated that the immobilization of $Pb^{2+}$ onto WAC-nZVI was favorable. From the comparison of the Langmuir monolayer adsorption capacities presented in Table 7, the WAC-nZVI performed effectively and distinctly than other existing nanoparticles and nanocomposites reported in the literature for the uptake of $Pb^{2+}$. This performance enlisted WAC-nZVI among novel, effective, and efficient adsorbents for uptake of $Pb^{2+}$. Based on the values of correlation coefficients ($R^2$), the close agreement between $q_{e,exp}$ and $q_{e,cal}$, and lower values of sum of square error (SSE), chi-square test ($\chi^2$), and normalized standard deviation ($\Delta q$) statistical validity models presented in Table 6, it is obvious that the equilibrium data were best described by Langmuir and D–R isotherm models and fairly described by Temkin isotherm models (Figure 10(a), (c), and (d), respectively).

Freundlich, Halsey, and Harkin–Jura are mainly describing heterogeneous and multilayer adsorption (*21*, *46*, *56*, *57*). Generally, these isotherm parameters are mainly determined from the slope and intercepts of their linear plots indicated in Table 5. The $K_f$ and $n_f$ are the Freundlich isotherm constants describing adsorption capacity and intensity, respectively, determined from the intercept and slope of the plot of log $q_e$ against log $C_e$ (Figure 10 (b)) . Since the value of $1/n_f$ (0.283 in Table 6) lies between 0 and 1 and $n_f$ (3.53, Table 6) being less than 10 are indication of a favorable adsorption. Adsorption of $Pb^{2+}$ onto WAC-nZVI is poorly described by Freundlich, Halsey, Harkin–Jura, and Jovanovic (Figure 10 (b), (e), (f), and (g), respectively, and Table 6). Based on $R^2$ and relatively low SEE, $\chi^2$, and $\Delta q$ presented in Table 6, the isotherm models fit the equilibrium data well in the following order: Langmuir > Dubinin–Raduskevich (D–R) > Temkin > Freundlich > Halsey > Jovanovic > Harkin–Jura. However, from the evaluated parameters of D–R isotherm models, the value of E being less than 8 kJ, revealed that electrostatic force played a substantial role in the adsorption process. This was supported by the research finding of Feng et al. (*42*) and Wang et al. (*48*).

**Table 6. Isotherm models' parameters and evaluated values for adsorption of $Pb^{2+}$ onto WAC-nZVI**

| Langmuir | Values | Freundlich | Values | Temkin | Values | D-R | Values |
|---|---|---|---|---|---|---|---|
| $q_{max}$ ($mgg^{-1}$) | 77.519 | $k_f$ | 32.885 | $b_T$ ($J\ mol^{-1}$) | 277.892 | $q_d$ | 82.163 |
| $K_L$ ($Lmg^{-1}$) | 1.344 | $1/n_f$ | 0.283 | $B$ ($Lg^{-1}$) | 8.916 | $A_{DKR}$ | $4 \times 10^{-8}$ |
| $R_L$ | $7.44 \times 10^{-2}$–$3.77 \times 10^{-3}$ | $n_f$ | 3.53 | $A_T$ ($Lg^{-1}$) | 180.925 | $E$ (J/mol) | 3,535.5 |
| $R^2$ | 0.972 | $R^2$ | 0.64 | $R^2$ | 0.842 | $R^2$ | 0.969 |
| SSE | 131.231 | SSE | 259.091 | SSE | 112.375 | SSE | 342.532 |
| $\chi^2$ | 1.748 | $\chi^2$ | 3.251 | $\chi^2$ | 1.514 | $\chi^2$ | 4.204 |
| $\Delta q$ | 4.502 | $\Delta q$ | 6.326 | $\Delta q$ | 4.166 | $\Delta q$ | 7.306 |
| Halsey | Values | Harkin–Jura | values | Jovanovic | values | | |
| $1/n_H$ | −0.283 | A | 133.33 | $q_{max}$ | 18.5061 | | |
| $n_H$ | −3.53 | $B$ | 1.0933 | $K_j$ | −0.0482 | | |
| $K_H$ | $4.42 \times 10^{-6}$ | 1/A | 0.0075 | | | | |
| $R^2$ | 0.6402 | $R^2$ | 0.3417 | $R^2$ | 0.45 | | |
| SSE | 259.693 | SSE | nd | SSE | 78.7266 | | |
| $\chi^2$ | 3.257 | $\chi^2$ | nd | $\chi^2$ | 0.8537 | | |
| $\Delta q$ | 6.333 | $\Delta q$ | nd | $\Delta q$ | 2.6616 | | |

Note: nd = non-determinate.

**Table 7. Comparison of the previously reported adsorbents used in $Pb^{2+}$ uptake with the present ones under investigation**

| S/N | Adsorbents | Adsorption capacity (mg/g) | Ref |
|---|---|---|---|
| 1 | Amino-functionalized $Fe_3O_4$-$SiO_2$ magnetic nanomaterial | 76.6 | (48) |
| 2 | Copolymer 2-hydroxyethyl methacrylate with monomer methyl methacrylate | 31.5 | (49) |
| 3 | Silica-supported dithiocarbamate | 70.4 | (50) |
| 4 | Nanometer $TiO_2$ | 22.5 | (51) |
| 5 | Exfoliated Graphene Nanosheets | 35.5 | (52) |
| 6 | Modified nanometer $SiO_2$ | 6 | (53) |
| 7 | Amino-functionalized mesoporous | 57.74 | (54) |
| Nanomesoporous silica | | | |
| 8 | Magnetic Chitosan/GO | 76.94 | (55) |
| 9 | WAC-nZVI | 77.5194 | Present study |

### *3.6. Adsorption thermodynamic studies*

Temperature is another important parameter in the adsorption studies because some important thermodynamic parameters such as enthalpy change ($\Delta H°$), entropy change ($\Delta S°$), and Gibbs free energy change ($\Delta G°$) could be determined. The temperature investigated ranged from 298 to 338 K. Close observation of Figure 11 revealed that 97.2% of $Pb^{2+}$ was adsorbed with an increase in temperature due to increase in number of active sites and the decrease in the thickness of the boundary layer surrounding the adsorbent, as a result, the mass transfer resistance of $Pb^{2+}$ in the boundary layer decreased (55)

The thermodynamic parameters were determined from the van't Hoff's equation (58):

**Figure 11. Effect of temperature on $Pb^{2+}$ adsorbed onto WAC-nZVI.**

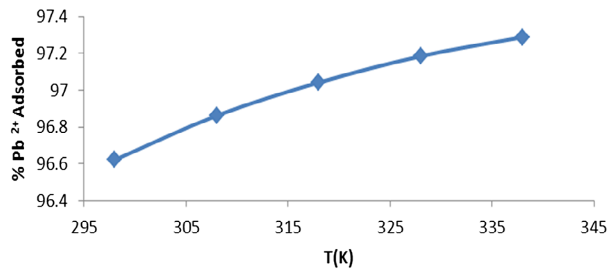


**Figure 12. Van't Hoff plot for the adsorption of $Pb^{2+}$ onto WAC-nZVI.**

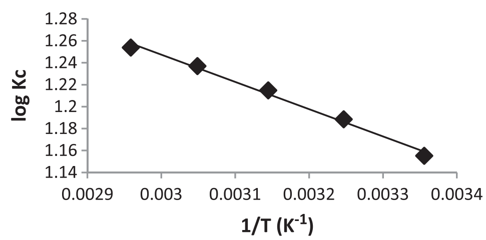


**Table 8. Thermodynamic parameters for adsorption of $Pb^{2+}$ onto WAC-nZVI**

| *T* (°C) | *T* (K) | Δ*G* (kJ mol⁻¹) | Δ*H* (kJ mol⁻¹) | Δ*S* (J mol⁻¹ K⁻¹) | $K_c$ |
|---|---|---|---|---|---|
| 25 | 298 | −6592 | 4.761 | 38.169 | 14.297 |
| 35 | 308 | −7009 | | | 15.434 |
| 45 | 318 | −7397 | | | 16.401 |
| 55 | 328 | −7769 | | | 17.262 |
| 65 | 338 | −8115 | | | 17.943 |

$$\log K_C = \frac{\Delta S}{2.303R} - \frac{\Delta H}{2.303RT} \tag{29}$$

Evaluated parameters of $\Delta H°$, $\Delta S°$, and $\Delta G°$ determined from the slope and intercept of linear plot of log $K_c$ against 1/T (Figure 12) are presented in Table 8.

It can therefore be ascertained from Table 8 that the reaction is endothermic because the value of ΔH is positive ($\Delta H = +4.761$ kJ mol⁻¹), the standard entropy change $\Delta S°$ (38.169 J mol⁻¹ K⁻¹) indicating the degree of randomness at the solid–liquid interface during the sorption of $Pb^{2+}$ onto WAC-nZVI and the negative values of the standard Gibbs free energy (ΔG°) indicate the viability, feasibility, and spontaneity of the adsorption process. This finding is in support with the report of other researchers (55).

### 3.7. Salinity/ionic strength

In waste water, salt is present in different concentrations depending on the source and quality of the effluent released into it. The presence of these dissolved salt and co-existing ions could affect the

**Figure 13. Ionic strength on $Pb^{2+}$ adsorbed onto WAC-nZVI.**

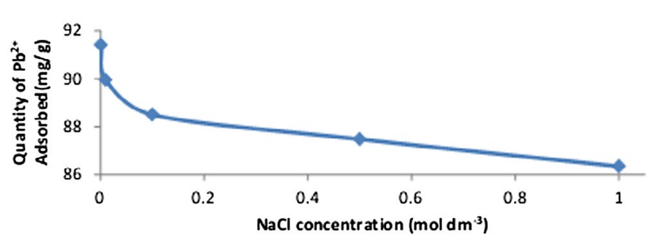


Notes: Experimental conditions: Pb2+ Concentration= 200 mg/L; Volume of Pb2+ Solution = 50 mL; WAC-nZVI dose = 100 mg; pH =6, contact time = 30 min, Stirring speed = 200 rpm and temperature = 25± 2°C.

adsorption of $Pb^{2+}$. Figure 13 depicts the result of effect of ionic strength on adsorption of $Pb^{2+}$ onto WAC-nZVI. It was obvious that the percentage of $Pb^{2+}$ removed reduced from 91.42 to 86.40%. This decrease in the amount of $Pb^{2+}$ uptake was due to electrostatic attraction arising from compressed electrical diffuse double layer. Also, increase in the number of $Pb^{2+}$, $Na^{+}$, and other competing ions led to electrostatic competition between $Pb^{2+}$ and $Na^{+}$ on the available adsorption sites which resulted to decrease in percentage of $Pb^{2+}$ removed (*21, 59*).

However, critical survey of the ranges of decrease in percentage did not show a drastic effect on the efficiency of WAC-nZVI in immobilization of $Pb^{2+}$ from the aqueous solution. Hence, WAC-nZVI nanocomposite could find relevance in adsorption of $Pb^{2+}$ from saline and natural water since 86.4% efficiency was obtained.

## 4. Conclusion

The immobilization of $Pb^{2+}$ onto WAC-nZVI vis-à-vis the kinetics, equilibrium, and thermodynamic studies was carried out successfully. The kinetic data were tested with eight kinetic and mechanism models. The kinetics was best described by pseudo-second-order, the adsorption mechanism was dominated by both intraparticle and external diffusions confirmed by Bangham and Boyd models. Of all the seven isotherm models investigated, equilibrium data analyzed fitted best to Langmuir isotherm models indicating that the interaction between $Pb^{2+}$ and WAC-nZVI was predominately chemisorption in nature. This was confirmed by the shift in bands from the FTIR spectra. However, electrostatic force played a substantial role in the adsorption process based on the D–R energy value, $E < 8$ k J $mol^{-1}$. Comparative investigation of the monolayer adsorption capacity of WAC-nZVI for $Pb^{2+}$ revealed that WAC-nZVI is a better nanoadsorbent with better performance than those previously reported. The result from the thermodynamic studies showed that immobilization of $Pb^{2+}$ was spontaneous, feasible, and endothermic in nature. Study of effect of ionic strength revealed that WAC-nZVI is a better candidate for industrial wastes in the presence of other competing ions. The immobilization of $Pb^{2+}$ by WAC-nZVI proved that it is an efficient and an effective nanoadsorbent and it is therefore recommended for utilization on large scale for decontamination of water and industrial treatment of effluent.

### Supplementary material
The supplementary material for this paper is available online at https://doi.org.10.1080/23312009.2017.1351653

### Acknowledgment
The serene environment and opportunity given to Dada, Adewumi Oluwasogo by both Landmark University and the University of Ilorin to undertake this doctoral research is highly appreciated. The assistance rendered by Ogunlaja Adeniyi in Rhodes University, South Africa for the SEM/EDX analyses is thankfully acknowledged.

### Funding
The authors received no direct funding for this research.

### Author details
Adewumi O. Dada[1]
E-mails: dada.oluwasogo@lmu.edu.ng, dada.oluwasogo@landmarkuniversity.edu.ng
Folahan A. Adekola[2]
E-mail: faadekola@yahoo.fr
Ezekiel O. Odebunmi[3]
E-mail: yibaf01@yahoo.com
[1] Department of Physical Sciences, Industrial Chemistry, Landmark University, P.M.B. 1001, Omu-Aran, Kwara State, Nigeria.
[2] Department of Industrial Chemistry, University of Ilorin, P.M.B. 1515, Ilorin, Nigeria.
[3] Department of Chemistry, University of Ilorin, P.M.B. 1515, Ilorin, Nigeria.

### Citation information
Cite this article as: Kinetics, mechanism, isotherm and thermodynamic studies of liquid-phase adsorption of Pb2+ onto wood activated carbon supported zerovalent iron (WAC-ZVI) nanocomposite, Adewumi O. Dada, Folahan A. Adekola & Ezekiel O. Odebunmi, *Cogent Chemistry* (2017), 3: 1351653.

### Cover image
Source: Authors

### References
(1) Järup, L. Hazards of Heavy Metal Contamination. *Br. Med. Bull.* 2003, *68*, 167–182. https://doi.org/10.1093/bmb/ldg032
(2) Yahaya, S. Lead Poisoning from Mining Kills 163 in Nigeria. *Reuters (Thomson Reuters)*, June 4, 2010. Retrieved 4 June 2010.
(3) Emeka, A. 28 Children Died of Lead Poisoning in Niger State. *The Guardian Newspaper*, Nigeria. Thursday May 14, 2015, http://www.grguardiannews.com/2015/05/28
(4) WHO. Lead. In: *Air quality guidelines for Europe*, 2nd ed.; World Health Organization Regional Office for Europe: Copenhagen, 2001. http://www.euro.who.int/__data/assets/pdf_file/0005/74732/E71922.pdf.
(5) WHO. *Lead exposure in children*. World Health Organization: Geneva, 2007. http://www.who.int/phe/news/Lead_in_Toys_note_060807.pdf.
(6) Dada, A.O.; Ojediran, J.O.; Olalekan, A.P. Sorption of $Pb^{2+}$ from Aqueous Solution unto Modified Rice Husk: Isotherms Studies. *Adv Phys Chem.* 2013**,** *2013*, 1–6. doi:10.1155/2013/842425.

(7) Cuizhen, S.; Jinwei, Q.; Zhibin, Z.; Taha, F.M.; Yanhao, Z.; Wen, Z. Characterization of Citric Acid Modified Clam Shells and Application for Aqueous Lead (II) Removal. *Water Air Soil Pollut.* 2016, *227*, 298. doi:10.1007/s11270-016-2975-z.

(8) Seul-Ji, L.; Jin, H.P.; Yong-Tae, A.; Jae, W.C. Comparison of Heavy Metal Adsorption by Peat Moss and Peat Moss-Derived Biochar Produced under Different Carbonization Conditions. *Water Air Soil Pollut.* 2015, *226*, 9. doi:10.1007/s11270-014-2275-4.

(9) Chen, X.; Jeyaseelan, S.; Graham, N. Physical and Chemical Properties Study of the Activated Carbon made from Sewage Sludge. *Waste Manage.* 2002, *22*, 775–760.

(10) Zhang, L.; Huang, T.; Zhang, M.; Guo, X.; Yuan, Z. Studies on the Capability and Behavior of Adsorption of Thallium on Nano-$Al_2O_3$. *J. Hazard. Mater.* 2008, *157*, 352–357. https://doi.org/10.1016/j.jhazmat.2008.01.005

(11) Jabeen, H.K.; Christian, K.K.; Chandra, V. Synthesis of Nano Zerovalent Iron Nanoparticles –Graphene Composite for the Treatment of Lead Contaminated Water. *J. Environ. Manage.* 2013, *130*, 429–435. https://doi.org/10.1016/j.jenvman.2013.08.022

(12) Hoch, L.B.; Mack, E.J.; Hydutsky, B.W.; Hershman, J.M.; Skluzacek, J.M.; Mallouk, T.E. Carbothermal Synthesis of Carbon-Supported Nanoscale Zero-Valent Iron Particles for the Remediation of Hexavalent Chromium. *Environ. Sci. Technol.* 2008, *42*, 2600–2605. https://doi.org/10.1021/es702589u

(13) Tseng, H.-H.; Su, J.-G.; Liang, G. Synthesis of Granular Activated Carbon/Zerovalent Iron Composites for Simultaneous Adsorption/Dechlorination of Trichloroethylene. *J. Hazard. Mater.* 2011, *192*, 500–506. https://doi.org/10.1016/j.jhazmat.2011.05.047

(14) Rodgers, P. Nanofabrication: Top down, Bottom up. *Nat. Nanotechnol.* 2006. doi:10.1038/nnano.2006.87.

(15) Dada, A.O.; Olalekan, A.P.; Olatunya, A.M.; Dada, O. Langmuir, Freundlich, Temkin and Dubinin-Radushkevich Isotherms Studies of Equilibrium Sorption of Zn2+ unto Phosphoric Acid Modified Rice Husk. *J. Appl. Chem.* 2012, *3* (2), 38–45.

(16) Dada, A.O.; Adekola, F.A.; Odebunmi, E.O. Isotherm, Kinetics and Thermodynamics Studies of Sorption of $Cu^{2+}$ onto Novel Zerovalent Iron Nanoparticles. *Covenant J Phys Life Sci.* 2014, *2* (1), 24–53.

(17) Dada, A.O.; Adekola, F.A.; Odebunmi, E.O. Kinetics and Equilibrium Models for Sorption of Cu(II) onto a Novel Manganese Nano-Adsorbent. *J. Dispersion Sci. Technol.* 2015, *37* (1), 119–133.

(18) Dada, A.O.; Latona, D.F.; Ojediran, J.O.; Osasuwa, N.O. Adsorption of Cu(II) onto Bamboo Supported Manganese (BS-Mn) Nanocomposite: Effect of Operational Parameters, Kinetic, Isotherms, and Thermodynamic Studies. *J. Appl. Sci. Environ. Manage.* 2016, *20* (2), 404–422.

(19) Srivastava, V.C.; Mall, I.D.; Mishra, I.M. Characterization of Mesoporous Rice Husk Ash (RHA) and Adsorption Kinetics of Metal Ions from Aqueous Solution onto RHA. *J. Hazard. Mater.* 2006, *134* (1–3), 257–267. https://doi.org/10.1016/j.jhazmat.2005.11.052

(20) Pyrzy′nska, K.; Bystrzejewski, M. Comparative Study of Heavy Metal Ions Sorption onto Activated Carbon, Carbon Nanotubes, and Carbon-Encapsulated Magnetic Nanoparticles. *Colloids. Sur.f A. Physicochem. Eng. Asp.* 2010, *362*, 102–109. https://doi.org/10.1016/j.colsurfa.2010.03.047

(21) Dada, A.O.; Adekola, F.A.; Odebunmi, E.O. A Novel Zerovalent Manganese for Removal of Copper Ions: Synthesis, Characterization and Adsorption Studies. *Appl. Water Sci.* 2015, *7*, 1409–1427. doi:10.1007/s13201-015-0360-5.

(22) Dada, A.O.; Adekola, F.A.; Odebunmi, E.O. Liquid Phase Scavenging of Cd (II) and Cu (II) Ions onto Novel Nanoscale Zerovalent Manganese (NZVMn): Equilibrium, Kinetic and Thermodynamic Studies. *Environ Nanotech Monitoring Manage.* 2017, *8*, 63–72. doi:10.1016/j.enmm.2017.05.001.

(23) Hameed, B.H. Equilibrium and Kinetic Studies of Methylviolet Sorption by Agricultural Waste. *J. Hazard. Mater.* 2008, *154* (1–3), 204–212. https://doi.org/10.1016/j.jhazmat.2007.10.010

(24) Foo, K.Y.; Hameed, B.H. Review: Insights into the Modeling of Adsorption Isotherm Systems. *Chem. Eng. J.* 2010, *156*, 2–10. https://doi.org/10.1016/j.cej.2009.09.013

(25) Boparai, H.K.; Meera, J.; Dennis, M.O. Kinetics and Thermodynamics of Cadmium Ion Removal by Adsorption onto Nano Zerovalent Iron Particles. *J. Hazard. Mater.* 2011, *186*, 458–465. https://doi.org/10.1016/j.jhazmat.2010.11.029

(26) Ahmad, M.A.; Puad, N.A.A.; Bello, O.S. Kinetic, Equilibrium and Thermodynamic Studies of Synthetic Dye Removal Using Pomegranate Peel Activated Carbon Prepared by Microwave-Induced KOH Activation. *Water Resour Industry.* 2014, *6*, 18–35. https://doi.org/10.1016/j.wri.2014.06.002

(27) Jaafar, M.Z.; Nasir, A.M.; Hamid, M.F. Point of Zero Charge for Sandstoneand Carbonate Rocks by Streaming Potential. *Int J Petrol Geosci Eng.* 2013, *1* (2), 82–90.

(28) Anees, A.M.; Rafatullah, O.S.; Mahamad, H.I.; Yap-Yee, C.; Bazlul, M.S. Removal of Cu(II) and Pb(II) Ions from Aqueous Solutions by Adsorption on Sawdust of Meranti Wood. *Desalination* 2009, *250*, 300–310.

(29) Sheela, T.; Nayaka, Y.A. Kinetics and Thermodynamics of Cadmium and Lead Ions Adsorption on NiO Nanoparticles. *Chem. Eng. J.* 2012, *191*, 123–131. https://doi.org/10.1016/j.cej.2012.02.080

(30) Oladipo, A.A.; Gazi, M. Uptake of $Ni^{2+}$ and Rhodamine B by Nano Hydroxyapatite/Alginate Composite Beads: Batch and Continuous-Flow Systems. *Toxicol. Environ. Chem.* 2015. doi:10.1080/02772248.2015.1115506.

(31) Xu, H.; Liu, Y.; Tay, J. Effect of PH on Nickel Biosorption by Aerobic Wood Sludge. *Biores. Technol.* 2006, *97* (3), 359–363. https://doi.org/10.1016/j.biortech.2005.03.011

(32) Pirouz, M.J.; Beyki, M.H.; Shemirani, F. Anhydride Functionalised Calcium Ferrite Nanoparticles: A New Selective Magnetic Material for Enrichment of Lead Ions from Water and Food Samples. *Food Chem.* 2015, *170*, 131–137. https://doi.org/10.1016/j.foodchem.2014.08.046

(33) Gong, J.; Chen, L.; Zeng, G.; Long, F.; Deng, J.; Niu, Q.; He, X. Shellac-Coated Iron Oxide Nanoparticles for Removal of Cadmium (II) Ions from Aqueous Solution. *J. Environ. Sci.* 2012, *24* (7), 1165–1173. https://doi.org/10.1016/S1001-0742(11)60934-0

(34) Ho, Y.-S. Removal of Copper Ions from Aqueous Solution by Tree Fern. *Water Res.* 2003, *37*, 2323–2330. https://doi.org/10.1016/S0043-1354(03)00002-2

(35) Chen, Z.-X.; Jin, X.-Y.; Chen, Z.; Megharaj, M.; Naidu, R. Removal of Methyl Orange from Aqueous Solution Using Bentonite-Supported Nanoscale Zerovalent Iron. *J. Colloid Interface Sci.* 2011, *363*, 601–607. https://doi.org/10.1016/j.jcis.2011.07.057

(36) Ho, Y.S.; Chiu, W.-T.; Hsu, C.-S.; Huang, C.-T. Sorption of Lead Ions from Aqueous Solution Using Tree Fern as a Sorbent. *Hydrometallurgy.* 2004, *73*, 55–61. https://doi.org/10.1016/j.hydromet.2003.07.008

(37) Song, C.; Wu, S.; Cheng, M.; Tao, P.; Shao, M.; Gao, G. Adsorption Studies of Coconut Shell Carbons Prepared by KOH Activation for Removal of Lead (II) from Aqueous Solutions. *Sustainability.* 2014, *6*, 86–98.

(38) Ayanda, O.S.; Fatoki, O. S.; Adekola, F.A.; Ximba, B.J. Kinetics and Equilibrium Models of the Sorption of Tributyltin to NZnO, Activated Carbon and NZnO/Activated Carbon Composite in Artificial Seawater. *Mar. Pollut. Bull.* 2013, *72* (1), 222–230. https://doi.org/10.1016/j.marpolbul.2013.04.001

(39) Bhatt, R.R.; Shah, B.A. Sorption Studies of Heavy Metal Ions by Salicylic Acid Formaldehyde–Catechol Terpoly-Meric Resin: Isotherm, Kinetic and Thermodynamics. *Arabian J. Chem.* 2015, *8* (3), 414–426. https://doi.org/10.1016/j.arabjc.2013.03.012
(40) Weber, W.J.; Morris, J.C. Kinetics of Adsorption on Carbon from Solution. *J. Sanit. Eng. Div. ASCE.* 1963, *89*, 31–59.
(41) Sun, X.-F.; Wang, S.-G.; Liu, X.-W.; Gong, W.-X.; Bao, N.; Gao, B.-Y.; Zhang, H.-Y. Biosorption of Malachite Green from Aqueous Solutions onto Aerobic Granules: Kinetic and Equilibrium Studies. *Biores. Technol.* 2008, *99*, 3475–3483. https://doi.org/10.1016/j.biortech.2007.07.055
(42) Feng, Q.; Lin, Q.; Gong, F.; Sugita, S.; Shoya, M. Adsorption of Lead and Mercury by Rice Husk Ash. *J. Colloid Interface Sci.* 2004, *278* (1), 1–8. https://doi.org/10.1016/j.jcis.2004.05.030
(43) Zhang, X.; Yu, H.; Yang, H.; Wan, Y.; Hu, H.; Zhai, Z.; Qin, J. Graphene Oxide Caged in Cellulose Microbeads for Removal of Malachite Green Dye from Aqueous Solution. *J. Colloid Interface Sci.* 2015, *437*, 277–282. https://doi.org/10.1016/j.jcis.2014.09.048
(44) Langmuir, I. The Adsorption of Gases on Plane Surfaces of Glass, Mica and Platinum. *J. Am. Chem. Soc.* 1918, *40*, 1361–1403.
(45) Zhou, Y.T.; Nie, H.L.; Branford-White, C.; He, Z.Y.; Zhu, L.M. Removal of $Cu^{2+}$ from Aqueous Solution by Chitosan-Coated Magnetic Nanoparticles Modified with Α-Ketoglutaric Acid. *J. Colloid Interface Sci.* 2009, *330*, 29–37. https://doi.org/10.1016/j.jcis.2008.10.026
(46) Harkins, W.D.; Jura, G.J. The Decrease of Free Surface Energy as a Basis for the Development of Equations for Adsorption Isotherms; and the Existence of Two Condensed Phases in Films on Solids. *J Chem. Phys.* 1944, *12*, 112–113. https://doi.org/10.1063/1.1723913
(47) Hao, Y.-M.; Chen, M.; Hu, Z.-B. Effective Removal of Cu(II) Ions from Aqueous Solution by Amino-Functionalized Magnetic Nanoparticles. *J. Hazard. Mater.* 2010, *184*, 392–399. https://doi.org/10.1016/j.jhazmat.2010.08.048
(48) Wang, J.; Zheng, S.; Shao, Y.; Liu, J. Amino-Functionalized $Fe_3O_4$–$SiO_2$ Core–Shell Magnetic Nanomaterial as a Novel Adsorbent for Aqueous Heavy Metals Removal. *J. Colloid Interface Sci.* 2010, *349*, 293–299. https://doi.org/10.1016/j.jcis.2010.05.010
(49) Bai, R.S.; Emilia, A. Studies on Chromium (VI) Adsorption-Desorption Using Immobilized Fungal Biomass. *Biores. Technol.* 2003, *87*, 17–26.
(50) Lian, N.; Chang, X.; Zheng, H.; Wang, X. Application of Nanometer $TiO_2$ in Adsorption of $Cr^{6+}$ and $Pb^{2+}$. *Microchem Acta.* 2005, *151*, 81–88. https://doi.org/10.1007/s00604-005-0381-0
(51) Huang, Z.-H.; Zheng, X.; Lv, W.; Wang, M.; Yang, Q.-H.; Kang, F. Adsorption of Lead Ions from Aqueous Solution on Low-Temperature Exfoliated Graphene Nanosheets. *Langmuir.* 2011, *27*, 7558–7562. https://doi.org/10.1021/la200606r
(52) Cai, X.; Gao, Y.; Sun, Q.; Chen, Z.; Megharaj, M.; Naidu, R. Removal of Co-Contaminants Cu (II) and Nitrate from Aqueous Solution Using Kaolin-Fe/Ni Nanoparticles. *Chem. Eng. J.* 2014, *244*, 19–26.
(53) Heidari, A.; Younesi, H.; Mehraban, Z.; Heikkinen, H. Selective Adsorption of Pb(II), Cd(II), and Ni(II) Ions from Aqueous Solution Using Chitosan–MAA Nanoparticles. *Int. J. Biol. Macromol.* 2013, *61*, 251–263. https://doi.org/10.1016/j.ijbiomac.2013.06.032
(54) Fan, L.L.; Luo, C.N.; Sun, M.; Li, X.J.; Qiu, H.M. Highly Selective Adsorption of Lead Ions by Water-Dispersible Magnetic/Graphene Oxide Composite. *Colloids Surface B.* 2013, *103*, 523–529. https://doi.org/10.1016/j.colsurfb.2012.11.006
(55) Doğan, M.; Türkyilmaz, A.; Alkan, M.; Demirbaş, Ö. Adsorption of Copper (II) Ions onto Sepiolite and Electrokinetic Properties. *Desalination.* 2009, *238*, 257–270.
(56) Basar, C.A. Applicability of the Various Adsorption Models of Three Dyes Adsorption onto Activated Carbon Prepared from Waste Apricot. *J. Hazard Mater.* 2006, *B135*, 232–241. https://doi.org/10.1016/j.jhazmat.2005.11.055
(57) Wang, L. Application of Activated Carbon Derived from 'Waste' Bamboo Culms for the Adsorption of Azo Disperse Dye: Kinetic, Equilibrium and Thermodynamic Studies. *J. Environ. Manage.* 2012, *102*, 79–87. https://doi.org/10.1016/j.jenvman.2012.02.019
(58) Lisha, K.P.; Shihabudheen, M.; Pradeep, M.T. Manganese Dioxide Nanowhiskers: A Potential Adsorbent for the Removal of Hg(II) from Water. *Chem. Eng. J.* 2010, *160*, 432–439. https://doi.org/10.1016/j.cej.2010.03.031
(59) Larous, S.; Meniai, A.-H.; Lehocine, B.M. Experimental Study of the Removal of Copper from Aqueous Solution by Adsorption Using Sawdust. *Desalination.* 2005, *185*, 483–490. https://doi.org/10.1016/j.desal.2005.03.090